Research Article Vol. 30, No. 17 / 15 Aug 2022 / *Optics Express* 29957

Optics EXPRESS

Phase-unwrapping-free 3D reconstruction in structured light field system based on varied auxiliary point

PING ZHOU,[1,*] YANZHENG WANG,[1] YUDA XU,[1] ZEWEI CAI,[2,3,4,5] AND CHAO ZUO[2,6]

[1] *School of Biological Science & Medical Engineering, Southeast University, Nanjing 210096, China*
[2] *Smart Computational Imaging Laboratory (SCILab), School of Electronic and Optical Engineering, Nanjing University of Science and Technolog, Nanjing, Jiangsu 210094, China*
[3] *Smart Computational Imaging Research Institute (SCIRI), Nanjing, Jiangsu Province 210019, China*
[4] *Jiangsu Key Laboratory of Spectral Imaging & Intelligent Sense, Nanjing, Jiangsu 210094, China*
[5] *zeweicai@njust.edu.cn*
[6] *zuochao@njust.edu.cn*
[*] *capzhou@163.com*

Abstract: Three-dimensional (3D) reconstruction is an essential task in structured light field (SLF) related techniques and applications. This paper presents a new method to reconstruct a 3D object point by using many auxiliary points adjacent to it. The relationship between two points in a SLF system is derived. Different from conventional "direct" methods that reconstruct 3D coordinates of the object point by using phase, slope, disparity *etc.,* the proposed method is an "indirect" method as the 3D coordinates of auxiliary points are not needed. Based on the auxiliary point theory, the wrapped phase obtained by 4-step phase-shifting method is sufficient for 3D reconstruction, without the need for phase unwrapping. To the best of our knowledge, this is the first strategy that combines the intrinsic characteristics of structured light and light field for phase-unwrapping-free 3D reconstruction. This paper also analyzes the constraints between system architecture parameters and phase rectification, phase to depth ratio, and presents a relatively simple criterion to guide the system design. Experimental results show that, with an appropriate system architecture, the proposed method can realize accurate, unambiguous, and reliable 3D reconstruction without phase unwrapping.

1. Introduction

Over the past decades, three-dimensional (3D) reconstruction has found wide applications in medicine, industry, etc., and various techniques have been proposed such as passive stereo vision and light field [1–7], active structured light [8–12] and structured light field [13–21]. Light field is a high-dimensional function that records 4D data and enables 3D reconstruction or depth estimation. Numerous algorithms have been developed based on the special properties of light field, including some matching-based methods [22,23], cues-based methods [24,25], EPI-based methods [6,26] and Learning-based methods [2,27]. As an upgraded version of structured light and light field technology, the structured light field (SLF) imaging has gained more and more attention due to the advantages of both structured light and light field characteristics, but at the cost of spatial resolution. A typical SLF imaging system consists of a projector and a light field camera. On one hand, compared to conventional structured light systems, the light field camera is able to record both spatial and angular distributions of light rays simultaneously when capturing fringe patterns modulated by objects. On the other hand, compared to passive light field technologies, the SLF imaging system benefits a lot from additional information of phase

#468049 https://doi.org/10.1364/OE.468049
Journal © 2022 Received 16 Jun 2022; revised 20 Jul 2022; accepted 20 Jul 2022; published 1 Aug 2022

encoding, and could achieve more accurate, real-time 3D reconstruction results. More cues have great potential to realize more distinguished 3D reconstruction.

Recently, many methods based on SLF have been proposed to achieve 3D reconstruction. In general, these methods use different strategies to combine different information that belongs to the structured light and light field. In 2016 and 2018, Zewei Cai, *et al.* [13,15] proposed a SLF imaging system using a Lytro light field camera instead of a 2D classical camera. After calibrating every light ray with spatial and angular parameters independently, 3D reconstruction was achieved based on phase mapping and ray constraint where the object points on a recorded light ray in light field are encoded by different phase. The method is a little similar to epipolar geometry principles, which combines angular information in light field and phase information in structured light, and uses angular information to eliminate phase ambiguity. A similar method was proposed by Feng, *et al*. [19] in 2021, where the sub-aperture image was extracted as multi-directional image first, and multi-directional phase-depth map was used for 3D reconstruction. Later, Cai, *et al*. carried out more studies and proposed different combination strategies for 3D reconstruction based on the SLF imaging system. In 2019, Cai, et al. [16] proposed angular defocus strategy that combines correspondence cue in the structured light and angular variance in the light field. The phase correspondence was used to search for non-ambiguous depths and the angular cue was weighted with phase to improve depth. In 2019, we also proposed a combination strategy for 3D reconstruction in the SLF imaging system [17,28]. We substituted phase consistency with radiance consistency in epipolar image, so that achieved 3D reconstruction after calibration. The combination strategy was also used by Xiang, *et al.* [21], but they used beetle antennae search optimization to determine the optimal slope in epipolar image. A single-shot 3D reconstruction method was also proposed by Cai, *et al*. [18]. The method uses defocus strategy and substitutes structured illumination with natural light variance directly, which is obtained by sinusoidal distribution in the fringe pattern. The strategy similar to defocusing was used by Fu, *et al*. [20] in their light-sheet based structured light field microscopy in 2021. They captured sinusoidal SLF images and proposed deconvolution and HiLo algorithms to achieve fast volumetric imaging.

The challenge of 3D reconstruction in the SLF imaging system is how to combine the structured light and light field information more effectively and perform 3D reconstruction more accurately. Therefore, new method or combination strategy is still an attractive research topic. This paper first introduces the Varied Auxiliary Point (VAP), and then proposes a new 3D reconstruction method to compute 3D coordinates of an object point by using the relationship between the object point and a large number of VAPs adjacent to it. The absolute unwrapped phase map is not required to distinguish these points since only the adjacent VAPs are used. In other words, the wrapped phase map is sufficient for 3D reconstruction, therefore phase unwrapping procedure is not needed. To the best of our knowledge, this is a new strategy of combining the characteristics of structured light and light field for phase-unwrapping-free 3D reconstruction. This paper also analyzes the constraints between system architecture and 3D reconstruction performance quantitatively, and presents a relatively simple parameter N to guide system design. Experimental results demonstrate the proposed Varied Auxiliary Point-based 3D reconstruction method and quantitative analysis for the SLF imaging system are effective and reliable.

2. Method

2.1. *VAP-based 3D reconstruction method*

The principal architecture of light field imaging model is divided into angular plane by the main lens and spatial plane by the MLA, as shown in Fig. 1. The angular plane and spatial plane are parallel to each other, which form the two-parallel-plane (TPP) model of the light field imaging system. Note that the scale of MLA in Fig. 1 is magnified to describe the imaging process clearly and only the focused light field camera is considered in this paper. The camera coordinate system $(O^c, X^cY^cZ^c)$ is defined as follows. Origin O^c is located at the optical center of the main lens,

Z^c-axis points towards the object space ($Z > 0$), and X^c and Y^c-axis point upward and out of the Fig. 1, respectively. The other coordinate systems used in this paper are described in Table 1 and follow the same convention as the coordinate system ($O^c, X^cY^cZ^c$).

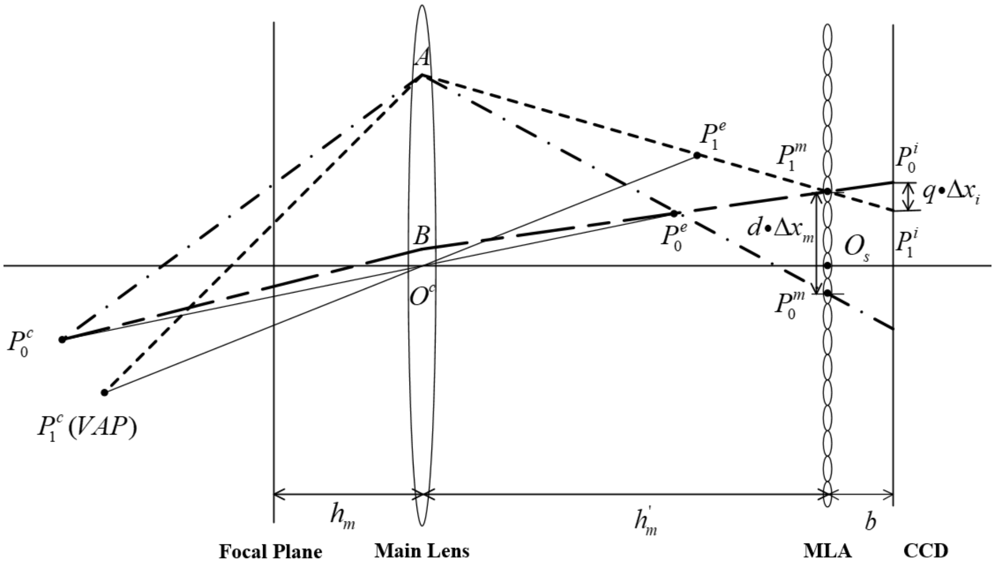

Fig. 1. VAP-based 3D reconstruction model.

Table 1. Notation of symbols in the light field model

$(O^c, X^cY^cZ^c)$	$O^m - X^mY^m$	$O^i - X^iY^iZ^i$
Camera coordinate system	MLA coordinate system	Image coordinate system
$O^w - X^wY^wZ^w$	$L(S, T, X, Y)$	$L(s, t, x, y)$
World coordinate system	Light field in TPP model	Decoded light field

Without loss of generality, let P_0 and P_1 denote two points in the object space of the main lens. All light rays emitted by P_0, P_1 pass through the main lens and converge at the image points P_0^e, P_1^e in the image space of the main lens, respectively. As shown in Fig. 1, some light rays of P_0, P_1 pass through a certain sub-aperture $A(s_a, t_a)$ of the main lens, where (s_a, t_a) are the coordinates of the sub-aperture in the main-lens, head to two microlens of MLA plane and converge at two image points $P_0^m(x_0^m, y_0^m)$, $P_1^m(x_1^m, y_1^m)$, respectively. Based on light field principles, P_0^m and P_1^m are in the same sub-aperture image $I_{(s_a,t_a)}(X, Y)$ that constructed by fixing angular coordinates as (s_a, t_a). In the microlens image $I_{(x_1^m,y_1^m)}(S, T)$ corresponding to P_1^m (constructed by fixing spatial coordinates as (x_1^m, y_1^m)), the light ray emitted by P_1 heads to P_1^i, which passes through sub-aperture A, P_1^e and P_1^m. Based on light field principles, an object point in the scene may appear multiple times in the image plane. We assume one of image points of P_0 is in the microlens image $I_{(x_1^m,y_1^m)}(S, T)$ and denoted as P_0^i, whose ray is emitted by P_0 and passes through another sub-aperture $B(s_b, t_b)$ and P_0^e. The assumption is true when P_0 and P_1 are close in the scene. In the sub-aperture image $I_{(s_a,t_a)}(X, Y)$, we define the distance between P_0^m and P_1^m is Δx_m pixels, and the distance between P_0^i and P_1^i in microlens image $I_{(x_1^m,y_1^m)}(S, T)$ is Δx_i pixels. Therefore, in the image space of the main lens, the distance between P_0^m and P_1^m is product of Δx_m and pitch d of microlens in MLA, and the distance between P_0^i and P_1^i is product of Δx_i and pixel size q of picture sensor, as shown in Fig. 1. More details about pitch d and pixel size q are shown in Fig. 3.

ΔABP_0^e and $\Delta P_1^m P_0^m P_0^e$, ΔABP_1^m and $\Delta P_1^i P_0^i P_1^m$ are both similar triangles, thus the relationship between the distances of the image points of P_1 and P_0 in sub-aperture image and microlens image can be drived as Eq. (1). Full details are given in Appendix 1.

$$\frac{q\Delta x_i}{d\Delta x_m} = -\frac{Z_0^e b}{(h'_m + Z_0^e)h'_m} \tag{1}$$

where Z_0^e is z-axis coordinate of P_0^e, h'_m is the distance between main lens and MLA, b is the distance between MLA and picture sensor. By re-writing Eq. (1), Z_0^e can be derived from the relationship between the image points of P_0 and P_1 in a sub-aperture image and a microlens image. Furthermore, as P_0^e is the image point of P_0, we could obtain Z_0^c by Gaussian formula in Geometrical optics and X_0^c, Y_0^c by the light field imaging principle, as depicted in Eq. (2).

$$\begin{cases} Z_0^c = \frac{qh'_m h_m k}{qh'_m k - h_m bd} \\ X_0^c = \frac{d}{h'_m}(x - x_0)Z_0^c \\ Y_0^c = \frac{d}{h'_m}(y - y_0)Z_0^c \end{cases} \tag{2}$$

where k is the ratio of Δx_i over Δx_m in Eq. (1), h_m is the distance between the focal plane of main lens and main lens plane, $O_s(x_0, y_0)$ are coordinates of the center point of the sub-aperture image. Therefore, for a point P_0 in the scene, as long as we find another point P_1 adjacent to it, we can derive the 3D coordinate of P_0 by determining their image points in a sub-aperture image and a microlens image, simultaneously. It is fundamental to the proposed method in this paper.

In SLF imaging system, we substitute 4D light field $\phi(s, t, x, y)$ with $L(s, t, x, y)$, where ϕ is the wrapped phase derived from the structured light. For a light ray $\phi(s_b, t_b, x_1, y_1)$ emitted by P_0, as shown in Fig. 1, its image point in the microlens image $I_{(x_1,y_1)}(S, T)$ is $P_0^i(s_b, t_b)$. We can pick another point $P_1^i(s_a, t_a)$ in this microlens image, then another light ray $\phi(s_a, t_a, x_1, y_1)$ emitted by P_1 is obtained. It's obvious that the image point of P_1 in the sub-aperture image $I_{(s_a,t_a)}(X, Y)$ is $P_1^m(x_1, y_1)$. In the same sub-aperture image, if the image point $P_0^m(x_0, y_0)$ is determined, we can obtain Z_0^e based on Eq. (1) by computing Δx_m and Δx_i.

In conventional phase-based 3D reconstruction method, it is necessary to get unwrapped absolute phase in the whole object to be measured. While in the proposed method, 3D reconstruction can be performed as long as two points can be distinguished in the microlens image and sub-aperture image. Based on light field principles, microlens image is the image that forms underneath a single microlens, which is a picture of small region of the scene. When the SLF imaging system is used, as the small region of microlens image is undoubtedly smaller than the wavelength of fringe pattern (the number of microlens is much more than that of fringe pattern periods), the wrapped phase is enough to distinguish two points not only in the microlens image but also in the sub-aperture image. Therefore, the phase unwrapping procedure is not required for our method. Furthermore, there are more than one point suitable to be P_1^i in a microlens image, and each P_1^i will lead to a measurement of Z_0^e. Measurement robustness and accuracy of P_0 can thus be improved by using optimization methods, such as linear regression. The proposed method uses P_1 to achieve the 3D reconstruction of P_0, but P_1 is varied and does not need to be measured, therefore, it is called ***varied auxiliary point***.

2.2. Phase rectification constraint

As mentioned above, this paper only uses wrapped phase to determine the image points of P_0 and P_1 in the sub-aperture image and microlens image. Unfortunately, many factors, such as vignetting, light consistence, etc., may introduce errors to the wrapped phase, thus lead to inaccurate 3D reconstruction of the SLF imaging system. The phase rectification is usually used to reduce errors [17]. Preliminary experimental result shows that the phase rectification performance is related to the equipment positions of the SLF imaging system, but the relationship between them is still not clear. In this section, a mathematic model is derived to describe the relationship between 3D reconstruction performance and the architecture of SLF imaging system.

According to Eq. (2), the depth of P_0 is related to the ratio of Δx_i to Δx_m. Let k_d denote the desired slope of the line composed by some pairs of $(\Delta x_m, \Delta x_i)$, as shown by the solid line in Fig. 2, then the depth ground truth can be deduced by k_d.

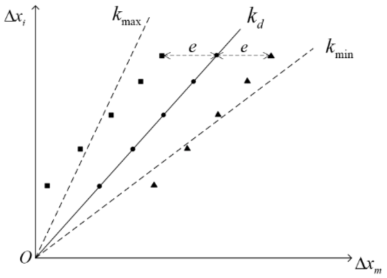

Fig. 2. Error analysis about phase rectification constraint

The wrapped phase error leads to P_0^m deviation in the sub-aperture image, thus decreases the accuracy of Δx_m. Let e denote the maximum error of Δx_m, then the maximum deviation of every pair of $(\Delta x_m, \Delta x_i)$ is $(\Delta x_m - e, \Delta x_i)$ (square points) or $(\Delta x_m + e, \Delta x_i)$ (triangle points), as shown in Fig. 2. Therefore, the real slope k corresponding to the desired k_d is in a certain upper and lower bounds $k_{\min}$ and $k_{\max}$ which can be derived as in Eq. (3). Full details are given in Appendix 2.

$$\begin{cases} k_{\min} = \frac{U_1k^2+U_2k}{U_3k^2+2U_1k+U_2} \\ k_{\max} = \frac{-U_1k^2+U_2k}{U_3k^2-2U_1k+U_2} \end{cases} \tag{3}$$

$$\begin{cases} U_1 = e\sum \Delta x_i^j \\ U_2 = \sum \Delta x_i^{j2} \\ U_3 = ne^2 \end{cases} \tag{4}$$

where n is the number of pairs of $(\Delta x_m, \Delta x_i)$ got in sub-aperture images and microlens images. As the function in Eq. (2) is monotonic, the depth Z_0 of P_0 is also bounded. For the sake of simplicity, only the mathematic model of $k_{\min}$ is derived in this section, and the model of $k_{\max}$ can be derived in the same way. In phase rectification, coordinates of P_0 are obtained from the real slope k based on Eq. (2) and re-projected to the projector plane, and the phase rectification principle constrains the scope of re-projection errors [17]. In other words, the maximum re-projector error in the projector plane caused by the maximum slope error is less than half fringe pattern wavelength. This relationship can be derived based on SLF imaging principles, which is described as follows

$$\left|\frac{N(ACU_3k_d^3 + ACU_1k_d^2)}{F_3k_d^3 + F_4k_d^2 + F_5k_d + F_6}\right| \le \frac{d_pw}{2h_p'T_N} \tag{5}$$

$$\begin{cases} F_3 = D_1A^2U_1 + 2D_2ABU_1 + D_2ACU_3 + D_3B^2U_1 + D_3BCU_3 \\ F_4 = D_1A^2U_2 + 2D_2ABU_2 + 3D_2ACU_1 + D_3B^2U_2 + 3D_3BCU_1 + D_3C^2U_3 \\ F_5 = 2D_2ACU_2 + 2D_3BCU_2 + 2D_3C^2U_1 \\ F_6 = D_3C^2U_2 \end{cases} \tag{6}$$

$$\begin{cases} N = \left[\frac{d}{h'_m} r_7(x-x_0) + \frac{d}{h'_m} r_8(y-y_0) + r_9\right] t_1 - \left[\frac{d}{h'_m} r_1(x-x_0) + \frac{d}{h'_m} r_2(y-y_0) + r_3\right] t_3 \\ D_1 = r_7^2 \frac{d^2}{h'^2_m}(x-x_0)^2 + 2r_7r_8\frac{d^2}{h'^2_m}(x-x_0)(y-y_0) + 2r_7r_9\frac{d}{h'_m}(x-x_0) \\ \qquad + r_8^2\frac{d^2}{h'^2_m}(y-y_0)^2 + 2r_8r_9\frac{d}{h'_m}(y-y_0) + r_9^2 \\ D_2 = r_7t_3\frac{d}{h'_m}(x-x_0) + r_8t_3\frac{d}{h'_m}(y-y_0) + r_9t_3 \\ D_3 = t_3^2 \\ A = qh'_m h_m \\ B = qh'^2_m \\ C = -h_m bd \end{cases} \tag{7}$$

where r_i and t_j are extrinsic parameters of the SLF imaging system, h'_p is the distance between the focal plane and main lens of the projector, d_p is the equivalent pixel size of projector's sensor, w is the number of pixels in the fringe pattern and T_N is the number of fringe periods, as shown in Fig. 3. According to Eq. (5), the re-projected point's position in the projector plane is related to coordinates of P_0, intrinsic and extrinsic parameters of the SLF imaging system. Therefore, the relationship in Eq. (5) specifies a constraint for the phase rectification method, which will fail when unreasonable system architecture is applied.

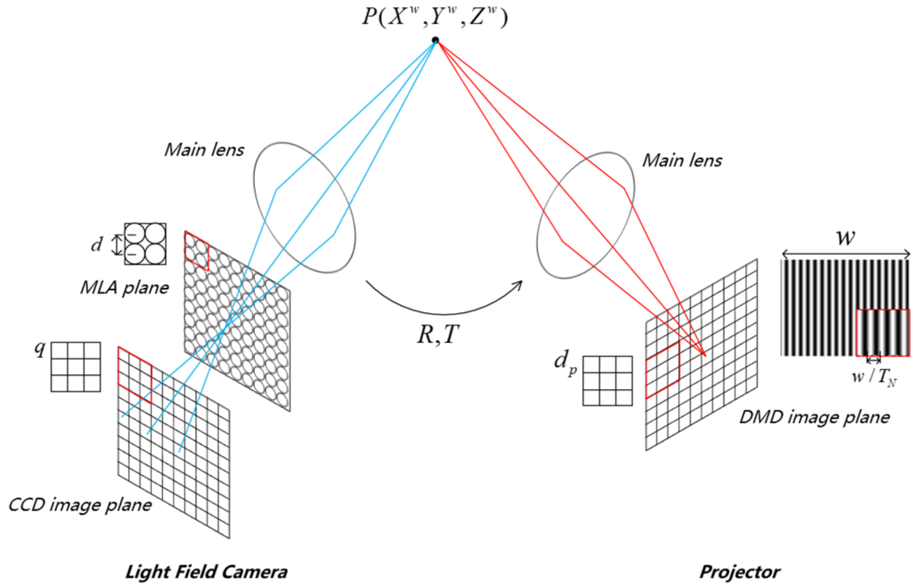

Fig. 3. The SLF imaging model

The relationship depicted in Eq. (5) is too complicated to determine each parameter of the SLF imaging system. However, it is not necessary to determine each parameter to meet the requirement of Eq. (5). t_1 in the translation matrix is related to N only, and N is related to the numerator of Eq. (5) only. Furthermore, t_1 and N are both not related to the denominator of Eq. (5). Therefore, it is possible to meet the requirement above by adjusting N only. To simplfy the problem, some assumptions regarding the system architecture are made. In general, the optical axes of the light field camera and projector are parallel to each other, and the fringe pattern is perpendicular to the system baseline, so that we assume the pitch angle and roll angle are both zero. Furthermore, by analyzing the parameters' order of magnitude, we simplify the description of N as follows

$$N \approx (10^{-1} r_7 + r_9)t_1 - (10^{-1} r_1 + r_3)t_3 \approx r_9 t_1 - r_3 t_3 \tag{8}$$

Finally, we obtain a relatively simple parameter N to describe the relationship between the system architecture and the 3D reconstruction performance. According to Eq. (5), the smaller N is, the easier phase rectification requirement can be met for better performance. According to Eq. (8), although N is still related to 4 parameters, we can adjust it by t_1 only to meet the requirement above. Therefore, by adjusting N, we can rectify errors due to vignetting etc. and improve 3D reconstruction.

2.3. Phase to depth ratio (PDR)

By determining appropriate system architecture, the phase rectification method can work well. However, due to ambient light condition, nonlinear gamma distortion, etc., some errors may still exist in the wrapped phase, which cannot be solved by the phase rectification method. This section, provides an instruction for designing an appropriate system architecture to decrease errors in the wrapped phase.

In general, when the object point is fixed, the more wrapped phase change, the better 3D reconstruction performance can be achieved. Similar to signal to noise ratio (SNR), phase to depth ratio (PDR) is used to describe this characteristics of the SLF imaging system. By analyzing the imaging procedure, PDR is approximatively expressed as follows. Full details are given in Appendix 3.

$$\left|\frac{\Delta\varphi}{\Delta Z}\right| \propto \frac{|N|}{|D_1 Z_1^2 + 2D_2 Z_1 + D_3|} \tag{9}$$

where N, D1 to D3 are shown in Eq. (7). As depicted in Eq. (9), PDR is a linear function about N. The bigger N is, the more PDR increases, so that we will achieve better performance of 3D SLF imaging. Similar to the analysis of phase rectification constraint, there is no need to determine every parameters in Eq. (9). Furthermore, compared with Eq. (5), it can be noticed that the phase rectification and PDR both depend on N, but their requirements are contradictory in theory, unfortunately. It seems that there is a dilemma about how to adjust these parameters to determine an appropriate system architecture. To meet the requirement of phase rectification constraint, smaller N is preferred, while smaller N will decrease PDR according to Eq. (9). In fact, N can be adjusted to a “median” value to meet both requirements of phase rectification and PDR simultaneously, then achieve acceptable results of SLF imaging.

3. Experimental results

3.1. VAP-based 3D reconstruction method

A SLF imaging system that mainly consists of a light field camera (Lytro Illum) and a digital projector (BENQ GP1) is constructed to verify our 3D reconstruction method and system analysis model, as shown in Fig. 4. The light field camera and projector are movably mounted to horizontal guides, along which we could adjust N as depicted in Eq. (5) and Eq. (9). In experiments, a periodic intensity fringe pattern presenting sinusoidal profile is projected onto the sculpture is as shown in Fig. 4. The periodic pattern and its shifted ones by a specific fraction of wavelength are recorded by the light field camera. Therefore, 4D raw digital images that contain 15×15 views are obtained, with a spatial resolution of 434×625 pixels each. In our SLF imaging system, the amount of shift is a one fourth of the total wavelength 2π.

The calibration of the SLF imaging system is performed by the two-step calibration [29] method proposed by us before. The calibration board is a pattern with 8 × 8 circles. After calibration, N and the other parameters in Eq. (5) and Eq. (9) are computed. To verify our 3D

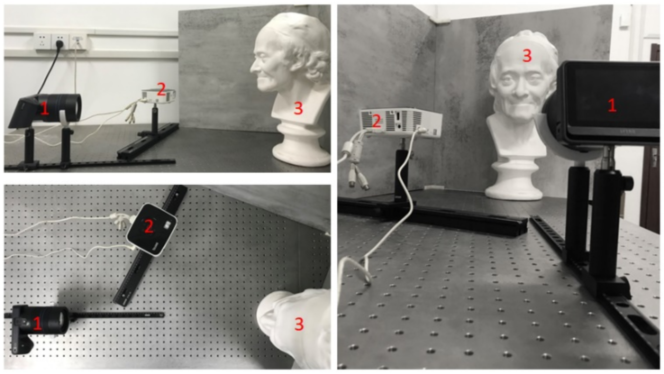

Fig. 4. The SLF imaging system

reconstruction method based on VAP, an EPI-based [17] method, and a 4-step phase-shifting and multi-frequency heterodyne method [30] are also used to reconstruct the same sculpture. The 3D reconstruction results computed by 4-step phase-shifting and multi-frequency heterodyne method are used as ground truth, according to the previous work [17]. The reconstructed point cloud computed by 3 different methods [17,30] are shown in Fig. 5. Note that all experiments are performed using the same SLF imaging system, whose intrinsic, extrinsic parameters are the same and shown in Table 2. In addition, the central sub-aperture image is used as reconstruction index, so that there exists one-to-one relationship among these reconstruction results by different methods.

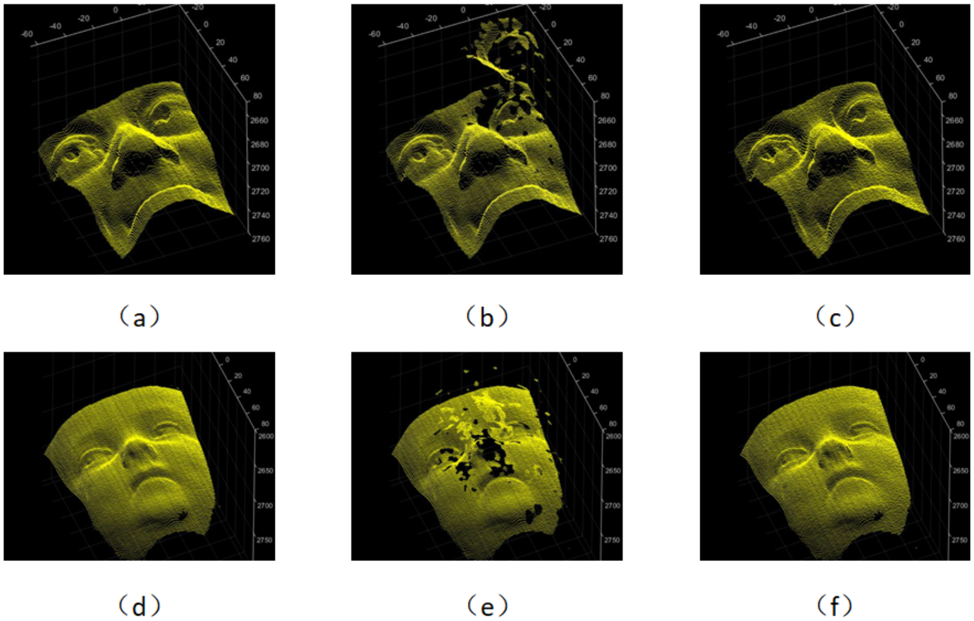
(a) (b) (c)
(d) (e) (f)

Fig. 5. 3D Reconstruction results by 3 methods. (a) (d) VAP. (b) (e) The EPI-based. (c) (f) 4-step phase-shifting and multi-frequency heterodyne method.

As shown in Fig. 5 (a) and (d), the reconstructed point cloud by our method is very similar to the ground truth in Fig. 5 (c) and (f), especially in regions with large depth changes, such

Table 2. Calibration parameters about Fig. 5

Parameter	Values	Parameter	Values
f	68.9335	$\begin{bmatrix} r_1 & r_2 & r_3 \\ r_4 & r_5 & r_6 \\ r_7 & r_8 & r_9 \end{bmatrix}$	$\begin{bmatrix} 0.9751 & 0.0089 & -0.2217 \\ -0.0045 & 0.9998 & 0.0203 \\ 0.2218 & -0.0188 & 0.9749 \end{bmatrix}$
h_m	2334	$\begin{bmatrix} t_1 & t_3 \end{bmatrix}$	$\begin{bmatrix} 672.2134 & -1159.2 \end{bmatrix}$
h'_m	71.0335	N	303.3333
d	0.0173	q	0.0014
b	0.0486		

as regions near canthus, nose and corner of mouth. To verify our method quantitatively, the mean distances between our results and ground truth are computed according to the one-to-one relationship and they are 0.55 mm and 0.33 mm only for the results in Fig. 5 (a) and (d). For the results by using EPI-based method as shown in Fig. 5 (b) and (e), although the point cloud around cheeks and forehead are smooth, large measurement errors are seen near eyes and the mean distance between the results in Fig. 5 (b) and (c) is 6.78 mm, the mean distance between the results in Fig. 5 (e) and (f) is to 6.28 mm. The experimental results demonstrate the ability of the proposed 3D reconstruction method to effectively reduce the point cloud measurement error.

3.2. Phase rectification constraint and PDR

To verify the phase rectification constraint and PDR, we change the system architecture and compare corresponding 3D reconstruction results. In these experiments, the sculpture and the light field camera are fixed all the time.

According to the analysis in Section 2, the projector is moved along the guide to adjust t_1 of the extrinsic matrix only, as shown in Fig. 4. Four typical 3D reconstruction results are shown from different viewpoints in Fig. 6, and their corresponding calibrated system parameters are shown in Table 3.

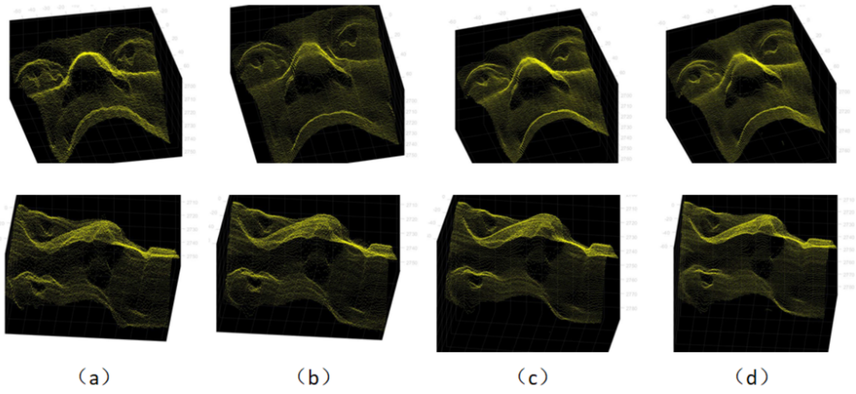
(a) (b) (c) (d)

Fig. 6. Experimental result with different N (from left to right, N increases)

As shown in Table 3, when t_1 increases, the other parameters are almost consistent. On one hand, some litter changes may occur inevitably when we move the projector although we do not want to change them, such as t_3, on the other hand, the global optimization in calibration may change some parameters a little. However, these changes should not affect our analysis about N too much. As shown in Table 3, N increases with t_1, thus the PDR increases according to Eq. (9).

Table 3. Calibration parameters about Fig. 6

	Group a	Group b	Group c	Group d
f	69.1011	69.0337	69.0975	68.9355
t_1	497.827	564.575	657.607	672.213
t_3	-1154.7	-1152.5	-1150	-1159.2
h_m	2348.9	2342	2340.1	2334
N	203.131	269.635	367.585	396.482
Mean Distance	0.97	0.69	0.55	0.55

It means that the ability is enhanced for phase to describe the depth change. Therefore, as PDR gets better, the 3D reconstruction results become smoother gradually, as shown in Fig. 6, which matches with the PDR analysis in Section 2.

Although PDR gets better as N increases, the phase rectification constraint may break when N is out of range. To further verify the phase rectification constraint and PDR, the same experiment was performed, where the focal length of the light field camera is adjusted so that the phase rectification constrain can be broken easier. The projector is moved along the guide to adjust t_1, the calibration parameters and reconstruction results are shown in Table 4 and Fig. 7, respectively.

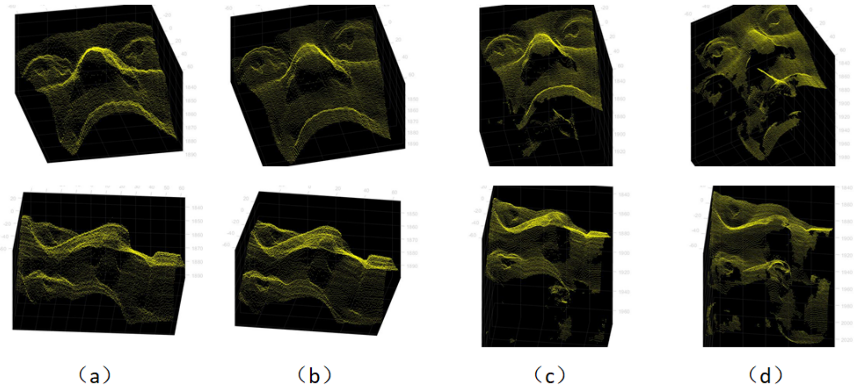

Fig. 7. Experimental result with different N where the focal length is different to that in Fig. 6. (from left to right, N increases)

Table 4. Calibration parameters about Fig. 7

	Group a	Group b	Group c	Group d
f	44.1125	44.1315	44.1971	44.0577
t_1	284.8760	337.2156	411.0217	536.3250
t_3	-351.7852	-354.2354	-348.7782	-343.3723
h_m	1526.9	1525.9	1528.6	1529.1
N	132.922	181.7774	250.1931	357.8807
Mean Distance	1.03	0.78	5.33	12.44

As shown in Fig. 7, the 3D reconstruction result is also getting smoother as N increases, which is consistent with previous experiments and PDR analysis. However, as mentioned in the analysis of phase rectification constrain in Section 2, it is necessary to hold the constraint to make the phase rectification available. When N is higher than a threshold, the phase rectification constrain will break inevitably. As shown in Fig. 7 (c) and (d), although point cloud are smoother than the results in Fig. 7 (a) and (b), there are apparent measurement errors. Furthermore, as N increases, larger measurement error in Fig. 7 (d) can be observed than Fig. 7 (c). The experimental results demonstrate the trade-off relationship between phase rectification constrain and PDR.

4. Conclusion and discussion

In summary, a new "indirect" 3D reconstruction method in SLF imaging system is proposed in this paper. Instead of measuring 3D coordinates of an object point directly, we accomplish measurement by the relationship between the object point and many points adjacent to it. The random errors due to performing measurement only once could be avoided. Furthermore, the wrapped phase is sufficient to distinguish adjacent points (the object points and VAPs), thus the phase unwrapping procedure is not required. To the best of our knowledge, it is a new strategy of combining the characteristics of structured light and light field for phase-unwrapping-free 3D reconstruction. In addition, to achieve accurate 3D reconstruction results, an instruction parameter N is introduced to guide the system design. Experimental results demonstrated that the proposed method is suitable for SLF imaging system and has the potential to accomplish 3D reconstruction. The primary disadvantage of SLF imaging system is the inherent trade-off between spatial and angular resolution (angular-spatial bandwidth) as the light field image is acquired at the cost of reduced spatial resolution. In addition, although our method is effective for 3D reconstruction in the SLF system, it does not work well in the passive light field system as there are not enough information to distinguish points in microlens images. Therefore, our future works will focus on the super-resolution algorithm, including learning-based algorithm and some effective strategies about distinguishing points in microlens images.

Funding. National Natural Science Foundation of China (52071075).

Disclosures. The authors declare no conflicts of interest, financial or otherwise.

Data availability. Data underlying the results presented in this paper are not publicly available at this time but may be obtained from the authors upon reasonable request.

Supplemental document. See Supplement 1 for supporting content.

References

1. Z. Ma, Z. Cen, and X. Li, "Depth estimation algorithm for light field data by epipolar image analysis and region interpolation," Appl. Opt. **56**(23), 6603–6610 (2017).
2. G. Wu, Y. Liu, L. Fang, Q. Dai, and T. Chai, "Light Field Reconstruction Using Convolutional Network on EPI and Extended Applications," IEEE Trans. Pattern Anal. Mach. Intell. **41**(7), 1681–1694 (2019).
3. H. G. Jeon, J. Park, G. Choe, J. Park, Y. Bok, Y. W. Tai, and I. S. Kweon, "Accurate depth map estimation from a lenslet light field camera," in *2015 IEEE Conference on Computer Vision and Pattern Recognition (CVPR)*, (2015), pp. 1547–1555.
4. T.-C. Wang, A. A. Efros, and R. Ramamoorthi, "Occlusion-Aware Depth Estimation Using Light-Field Cameras," in *2015 IEEE International Conference on Computer Vision (ICCV)*, (2015), pp. 3487–3495.
5. S. Zhang, H. Sheng, C. Li, J. Zhang, and Z. Xiong, "Robust depth estimation for light field via spinning parallelogram operator," Comput. Vis. Image Understanding **145**, 148–159 (2016).
6. J. Chen, J. Hou, Y. Ni, and L. P. Chau, "Accurate Light Field Depth Estimation With Superpixel Regularization Over Partially Occluded Regions," IEEE Trans. on Image Process. **27**(10), 4889–4900 (2018).
7. I. K. Williem, K. M. Park, and Lee, "Robust Light Field Depth Estimation Using Occlusion-Noise Aware Data Costs," IEEE Trans. Pattern Anal. Mach. Intell. **40**(10), 2484–2497 (2018).
8. Z. Li, K. Zhong, Y. F. Li, X. Zhou, and Y. Shi, "Multiview phase shifting: a full-resolution and high-speed 3D measurement framework for arbitrary shape dynamic objects," Opt. Lett. **38**(9), 1389–1391 (2013).
9. Y. An, J. S. Hyun, and S. Zhang, "Pixel-wise absolute phase unwrapping using geometric constraints of structured light system," Opt. Express **24**(16), 18445–18459 (2016).
10. T. Tao, Q. Chen, S. Feng, Y. Hu, J. Da, and C. Zuo, "High-precision real-time 3D shape measurement using a bi-frequency scheme and multi-view system," Appl. Opt. **56**(13), 3646–3653 (2017).
11. G. Wu, Y. Wu, L. Li, and F. Liu, "High-resolution few-pattern method for 3D optical measurement," Opt. Lett. **44**(14), 3602–3605 (2019).
12. W. Li, N. Fan, Y. Wu, G. Wu, S. Yang, H. Huang, Y. Yang, T. Yang, and F. Liu, "Fringe-width encoded patterns for 3D surface profilometry," Opt. Express **29**(21), 33210–33224 (2021).

Optics EXPRESS

13. Z. Cai, X. Liu, X. Peng, Y. Yin, A. Li, J. Wu, and B. Z. Gao, "Structured light field 3D imaging," Opt. Express **24**(18), 20324–20334 (2016).
14. Z. Cai, X. Liu, Z. Chen, Q. Tang, B. Z. Gao, G. Pedrini, W. Osten, and X. Peng, "Light-field-based absolute phase unwrapping," Opt. Lett. **43**(23), 5717–5720 (2018).
15. Z. Cai, X. Liu, X. Peng, and B. Z. Gao, "Ray calibration and phase mapping for structured-light-field 3D reconstruction," Opt. Express **26**(6), 7598–7613 (2018).
16. Z. Cai, X. Liu, G. Pedrini, W. Osten, and X. Peng, "Accurate depth estimation in structured light fields," Opt. Express **27**(9), 13532–13546 (2019).
17. P. Zhou, Y. T. Zhang, Y. L. Yu, W. J. Cai, and G. Q. Zhou, "3D shape measurement based on structured light field imaging," Math. Biosci. Eng. **17**(1), 654–668 (2020).
18. Z. Cai, G. Pedrini, W. Osten, X. Liu, and X. Peng, "Single-shot structured-light-field three-dimensional imaging," Opt. Lett. **45**(12), 3256–3259 (2020).
19. W. Feng, T. Qu, J. Gao, H. Wang, X. Li, Z. Zhai, and D. Zhao, "3D reconstruction of structured light fields based on point cloud adaptive repair for highly reflective surfaces," Appl. Opt. **60**(24), 7086–7093 (2021).
20. Z. Fu, Q. Geng, J. Chen, L. A. Chu, A. S. Chiang, and S. C. Chen, "Light field microscopy based on structured light illumination," Opt. Lett. **46**(14), 3424–3427 (2021).
21. S. Xiang, L. Liu, H. Deng, J. Wu, Y. Yang, and L. Yu, "Fast depth estimation with cost minimization for structured light field," Opt. Express **29**(19), 30077–30093 (2021).
22. K. Yucer, C. Kim, A. Sorkine-Hornung, and O. Sorkine-Hornung, "Depth from Gradients in Dense Light Fields for Object Reconstruction," in *2016 Fourth International Conference on 3D Vision (3DV)*, (2016), pp. 249–257.
23. S. Heber and T. Pock, "Shape from Light Field Meets Robust PCA," in *European Conference on Computer Vision*, (2014), pp. 751–767.
24. H. Lin, C. Chen, S. B. Kang, and J. Yu, "Depth Recovery from Light Field Using Focal Stack Symmetry," in *2015 IEEE International Conference on Computer Vision (ICCV)*, (2015), pp. 3451–3459.
25. W. Williem and I. K. Park, "Robust Light Field Depth Estimation for Noisy Scene with Occlusion," in *2016 IEEE Conference on Computer Vision and Pattern Recognition (CVPR)*, (2016), pp. 4396–4404.
26. T. Suzuki, K. Takahashi, and T. Fujii, "Disparity estimation from light fields using sheared EPI analysis," in *2016 IEEE International Conference on Image Processing (ICIP)*, (2016), pp. 1444–1448.
27. J. Chen, J. Hou, and L.-P. Chau, "Light Field Denoising via Anisotropic Parallax Analysis in a CNN Framework," IEEE Signal Process. Lett. **25**(9), 1403–1407 (2018).
28. P. Zhou, Z. Yang, W. Cai, Y. Yu, and G. Zhou, "Light field calibration and 3D shape measurement based on epipolar-space," Opt. Express **27**(7), 10171–10184 (2019).
29. P. Zhou, W. Cai, Y. Yu, Y. Zhang, and G. Zhou, "A two-step calibration method of lenslet-based light field cameras," Opt. Lasers Eng. **115**, 190–196 (2019).
30. N. Karpinsky, C. Quan, S. Lei, K. Qian, A. K. Asundi, S. Zhang, and F. S. Chau, "High-resolution, real-time fringe pattern profilometry," Proc. SPIE **7522**, 75220E (2010).